The Meteoritical Society

Meteoritics & Planetary Science 49, Nr 9, 1612–1625 (2014)
doi: 10.1111/maps.12208

Stardust Interstellar Preliminary Examination VI: Quantitative elemental analysis by synchrotron X-ray fluorescence nanoimaging of eight impact features in aerogel

Alexandre S. SIMIONOVICI[1*], Laurence LEMELLE[2], Peter CLOETENS[3], Vicente A. SOLÉ[3], Juan-Angel Sans TRESSERAS[3], Anna L. BUTTERWORTH[4], Andrew J. WESTPHAL[4], Zack GAINSFORTH[4], Julien STODOLNA[4], Carlton ALLEN[5], David ANDERSON[4], Asna ANSARI[6], Saša BAJT[7], Nabil BASSIM[8], Ron K. BASTIEN[5], Hans A. BECHTEL[9], Janet BORG[10], Frank E. BRENKER[11], John BRIDGES[12], Donald E. BROWNLEE[13], Mark BURCHELL[14], Manfred BURGHAMMER[3], Hitesh CHANGELA[15], Andrew M. DAVIS[16], Ryan DOLL[17], Christine FLOSS[17], George FLYNN[18], David R. FRANK[5], Eberhard GRÜN[19], Philipp R. HECK[6], Jon K. HILLIER[20], Peter HOPPE[21], Bruce HUDSON[22], Joachim HUTH[21], Brit HVIDE[6], Anton KEARSLEY[23], Ashley J. KING[16], Barry LAI[24], Jan LEITNER[19], Ariel LEONARD[17], Hugues LEROUX[25], Robert LETTIERI[4], William MARCHANT[4], Larry R. NITTLER[26], Ryan OGLIORE[27], Wei Ja ONG[17], Frank POSTBERG[20], Mark C. PRICE[14], Scott A. SANDFORD[28], Sylvia SCHMITZ[11], Tom SCHOONJANS[29], Geert SILVERSMIT[29], Ralf SRAMA[30], Frank J. STADERMANN[17], Thomas STEPHAN[16], Veerle J. STERKEN[21,30,31], Rhonda M. STROUD[32], Steven SUTTON[24], Mario TRIELOFF[20], Peter TSOU[33], Akira TSUCHIYAMA[34], Tolek TYLISZCZAK[9], Bart VEKEMANS[29], Laszlo VINCZE[29], Joshua Von KORFF[4], Naomi WORDSWORTH[35], Daniel ZEVIN[4], Michael E. ZOLENSKY[5], and > 30,000 Stardust@home dusters[36]

[1]Institut des Sciences de la Terre, Observatoire des Sciences de l'Univers de Grenoble, Grenoble, France
[2]LGL-LJC, CNRS, Ecole Normale Supérieure de Lyon, Lyon, France
[3]European Synchrotron Radiation Facility, Grenoble, France
[4]Space Sciences Laboratory, U.C. Berkeley, Berkeley, California, USA
[5]ESCG, NASA JSC, Houston, Texas, USA
[6]Robert A. Pritzker Center for Meteoritics and Polar Studies, The Field Museum of Natural History, Chicago, Illinois, USA
[7]DESY, Hamburg, Germany
[8]Naval Research Laboratory, Washington, District of Columbia, USA
[9]Advanced Light Source, Lawrence Berkeley Laboratory, Berkeley, California, USA
[10] Retired IAS Orsay, Orsay, France
[11]Geoscience Institute, Goethe University Frankfurt, Frankfurt, Germany
[12]Space Research Centre, University of Leicester, Leicester, UK
[13]Department of Astronomy, University of Washington, Seattle, Washington, USA
[14]School of Physical Sciences, University of Kent, Canterbury, Kent, UK
[15]Physics Deparrment, George Washington University, Washington, District of Columbia, USA
[16]Department of the Geophysical Sciences, University of Chicago, Chicago, Illinois, USA
[17]Physics Department, Washington University, St. Louis, Missouri, USA
[18]SUNY Plattsburgh, Plattsburgh, New York, USA
[19]Max-Planck-Institut für Kernphysik, Heidelberg, Germany
[20]Institut für Geowissenschaften, Universität Heidelberg, Heidelberg, Germany
[21]Max-Planck-Institut für Chemie, Mainz, Germany
[22]Ontario, Canada
[23]Natural History Museum, London, UK
[24]Advanced Photon Source, Argonne National Laboratory, Chicago, Illinois, USA
[25]Université des Sciences et Technologies de Lille, France
[26]Carnegie Institution of Washington, Washington, District of Columbia, USA
[27]Institute of Geophysics and Planetology, University of Hawai'i at Manoa, Honolulu, Hawai'i, USA
[28]NASA Ames Research Center, Moffet Field, California, USA

[29]University of Ghent, Ghent, Belgium
[30]Institut für Raumfahrtsysteme, University Stuttgart, Stuttgart, Germany
[31]IGEP, TU Braunschweig, Braunschweig, Germany
[32]Materials Science and Technology Division, Naval Research Laboratory, Washington, District of Columbia, USA
[33]Jet Propulsion Laboratory, Pasadena, California, USA
[34]Department of Earth and Space Science, Osaka University, Osaka, Japan
[35]South Buckinghamshire, UK
[36]Worldwide
*Corresponding author. E-mail: Alexandre.Simionovici@ujf-grenoble.fr

(Received 29 December 2012; revision accepted 05 August 2013)

Abstract–Hard X-ray, quantitative, fluorescence elemental imaging was performed on the ID22NI nanoprobe and ID22 microprobe beam lines of the European Synchrotron Research facility (ESRF) in Grenoble, France, on eight interstellar candidate impact features in the framework of the NASA Stardust Interstellar Preliminary Examination (ISPE). Three features were unambiguous tracks, and the other five were identified as possible, but not definite, impact features. Overall, we produced an absolute quantification of elemental abundances in the $15 \leq Z \leq 30$ range by means of corrections of the beam parameters, reference materials, and fundamental atomic parameters. Seven features were ruled out as interstellar dust candidates (ISDC) based on compositional arguments. One of the three tracks, I1043,1,30,0,0, contained, at the time of our analysis, two physically separated, micrometer-sized terminal particles, the most promising ISDCs, Orion and Sirius. We found that the Sirius particle was a fairly homogenous Ni-bearing particle and contained about 33 fg of distributed high-Z elements ($Z > 12$). Orion was a highly heterogeneous Fe-bearing particle and contained about 59 fg of heavy elements located in hundred nanometer phases, forming an irregular mantle that surrounded a low-Z core. X-ray diffraction (XRD) measurements revealed Sirius to be amorphous, whereas Orion contained partially crystalline material (Gainsforth et al. 2014). Within the mantle, one grain was relatively Fe-Ni-Mn-rich; other zones were relatively Mn-Cr-Ti-rich and may correspond to different spinel populations. For absolute quantification purposes, Orion was assigned to a mineralogical assemblage of forsterite, spinel, and an unknown Fe-bearing phase, while Sirius was most likely composed of an amorphous Mg-bearing material with minor Ni and Fe. Owing to its nearly chondritic abundances of the nonvolatile elements Ca, Ti, Co, and Ni with respect to Fe, in combination with the presence of olivine and spinel as inferred from XRD measurements, Orion had a high probability of being extraterrestrial in origin.

INTRODUCTION

The Stardust sample return mission collection (Tsou et al. 2003; Brownlee et al. 2006) provided a unique opportunity for capture and return of the first samples of contemporary interstellar dust. It provides a sensitive test of our knowledge of the abundances and distribution of the elements in the interstellar medium (ISM). So far, interpretations of astronomical observations of the ISM (Sofia and Meyer 2001) indicate that many heavy elements ($Z > 8$) were concentrated in dust grains (Kimura et al. 2003; Jenkins 2008; Mann 2010). In addition, analyses of local, contemporary interstellar dust carried out at the same scale as analyses performed on cometary (Schramm et al. 1989; Flynn et al. 2006) and presolar samples (Lodders and Amari 2005) offer an opportunity of investigating the similarities between the present local interstellar cloud (LIC) and the early solar nebula (Mumma and Charnley 2011) and estimating the possibilities of matter exchange between the LIC and the presolar molecular cloud from which our solar system was formed about 4.57 billion years ago (Frisch and Slavin 2012).

In this work, our interstellar preliminary examination (ISPE; Westphal et al. 2014a, 2014b) team reported on noninvasive analyses by synchrotron X-ray fluorescence (XRF) carried out on both the ID22NI nanoimaging and ID22 microimaging endstations at the ESRF in Grenoble, France, on eight candidate impact features, with a particular focus on two possible ISDCs, found in track I1043,1,30,0,0.

SAMPLES AND SYNCHROTRON EXPERIMENTAL SETUP

Analyzed features were identified by volunteers of the Stardust@home initiative (Westphal et al. 2005, 2010, 2014a, 2014b) and extracted at NASA's Johnson Space Center in Houston, Texas (Frank et al. 2013). After extraction, IS candidates were imaged directly in picokeystones, prepared from the original Stardust low-density (0.02–0.04 g cm^{-3}) silica aerogel capture medium. The picokeystones were confined within containers consisting of two 70 nm Si3N4 membranes (Westphal et al. 2010).

The ESRF ID22NI and ID22 are two branches of the same beam line, dedicated to nano- and microimaging, respectively. The ID22NI nanoimaging endstation (Bleuet et al. 2008) is located 64 m downstream of an in-vacuum high-flux undulator covering the 7–70 keV energy range. A piezoelectric drive for sample scanning in three dimensions was coupled to a stepper-motor goniometer for powder XRD angular scans. An ESRF-designed, highly optimized Kirkpatrick-Baez bent mirror assembly was used for focusing the synchrotron X-ray beam to a spot 50–250 nm FWHM (full width half maximum) in both the vertical and horizontal dimensions. The incident and transmitted photon fluxes were measured with an ionization chamber and PIN Si photodiode detector, respectively. A fixed-exit, Si 111/Si 311 double crystal Kohzu monochromator was used for monochromatization in the energy range 7–30 keV. The ID22 microprobe had a similar setup, only 22 m closer to the insertion device, thus featuring beam spots in the 1–5 μm range. For some of our particles, to ensure high flux and fast dwell time per point, the high-intensity "pink" beam mode was employed. In this mode, a full undulator harmonic, filtered through a thin CVD diamond absorber, was directly focused onto the sample, after a plane mirror reflection to cut off higher energy X-rays. The beam had an energy bandwidth of approximately 1.5% at the incident energy of 17 keV for intensities of up to 2×10^{12} ph s^{-1} in an approximately square 200 nm beam spot. X-ray fluorescence (XRF), XRD, and X-ray computed tomography (XCT) analyses can be performed at high spatial resolution and fast scanning time. We scanned the samples simultaneously collecting both XRF and XRD data (reported in Gainsforth et al. 2014).

Using a 17 keV beam of 7×10^{11} ph s^{-1}, the NIST SRM 1577 (standard reference materials) bovine liver reference material for absolute quantification, coupled to our ESRF PyMCA fluorescence analysis code (Sole et al. 2007) and to our Xraylib fluorescence cross section database (Brunetti et al. 2004), minimum detection limits (MDL) of about 90 zg (zeptograms = 10^{-21} g) and 50 zg were obtained for Z = 30 (Zn) and Z = 34 (Se), respectively, for a 300 s acquisition. The MDL is background-controlled, even though the background is low, so mapping with a shorter, 1s dwell time per pixel then yielded an MDL of about 1.6 ag (attograms = 10^{-18} g) in the region of Z = 30. The standard served only to measure a figure for the absolute incident flux on the sample, which must be measured in the same experimental conditions as the Stardust particles. We used Fe, present at well-quantified trace element values in SRM 1577, as the reference element, which allowed direct quantification, while all other elements were quantified by scaling our Xraylib fluorescence cross section ratios versus the sample element normalized to the measured Fe ratios.

The quantification procedure made use of the low Z STXM Mg and Al results from Orion and Sirius, obtained by Butterworth et al. (2014) using the scanning transmission X-ray microscopy (STXM) beam line 11.0.2 at the Advanced Light Source synchrotron (ALS), Lawrence Berkeley National Laboratory. This instrument is optimized for high spatial resolution mapping and spectroscopy of C, O, Mg, Al, Si, Fe, and Ni in particles and impact features. An elliptical undulator coupled to a plane-grating monochromator delivers few nanometer-sized beams in the energy range 80–2000 eV, with a $\Delta E/E$ resolving power of about 3500.

We used the knife-edge method to determine that the beam size FWHM was 224 nm horizontal by 234 nm vertical. For the final mapping, the sample was scanned in 152 nm (horizontal) by 153.8 nm (vertical) steps, with a dwell time of 8 seconds, to extract the actual number of fluorescence counts.

XRF DATA ANALYSIS

For every particle identified in the fluorescence maps, a single average spectrum was produced using the PyMCA imaging set of commands. A contour of the particle was outlined using Fe as the contrasting element. All the individual spectra of pixels inside the contour were then averaged to produce the final average particle spectrum. The contribution from the aerogel within the particle contour was then subtracted from the total particle spectrum, to derive a background-corrected average particle spectrum. As aerogel is a heterogeneous medium, an average of six aerogel areas from the map in the immediate vicinity of the particles were used to produce an average, pixel-normalized, local aerogel spectrum. PyMCA analyses of the total spectra were performed for all terminal particles and some tracks, yielding an absolute mass quantification of the particles and mass fractions of each fitted element. This can be carried out only if the

elemental composition of the particle matrix (layered or homogeneous) is defined (here considered homogenous) as well as the particle density and thickness. As X-ray attenuation and measurements of total mass and mass ratios depend on the matrix composition, we investigated the sensitivity of our results to changes in the composition and density of the matrix. Matrix corrections were calculated for particles embedded between double layers (thickness 2×35 μm) of homogeneous aerogel. Where possible, the absolute masses per element were derived from the current mass fractions using the total particle masses and densities estimated by Butterworth et al. (2014).

ERROR TREATMENT

When quantifying XRF data, one must address all sources of error, in particular the ones related to fundamental parameters such as the absolute fluorescence cross sections or the uncertainties associated with the fluorescence reference materials, as well as the X-ray beam parameters (size, fluence, energy bandwidth). Here, we use all sources of error to derive confidence intervals, as follows: (1) the SRM 1577b standard is prepared from freeze-dried powdered bovine liver tissue pelletized to a thickness of 150 ± 15 μm with a laboratory press. This multielement standard contains approximately 90% of an undetected $C_6H_{12}O_6$ organic base and 17 other fitted elements at several tens to hundreds of ppm concentrations. Fe, used as a primary reference element, is present at 184 ± 15 ppm. (2) Based on the standard Fe concentration and the moderate-to-low absorption featured for all fitted elements, one obtains a figure for absolute quantification of samples containing Fe. To extend this quantification to other elements, we used the ratio of fluorescence cross sections of Fe to the element to be calibrated extracted from our Xraylib cross sections (Brunetti et al. 2004). As the estimated uncertainties of the cross sections were about 5% (Krause et al. 1978), their ratios, following error propagation techniques, had a total uncertainty of approximately 7%. This was summed up in quadrature with the statistical errors and peak fitting errors reported by PyMCA for all Z except Fe. All uncertainties were propagated throughout the whole quantification process, including the total Al and Mg masses and uncertainties derived from STXM measurements by Butterworth et al. (2014). Calculated ratios made use of the fact that Fe, the reference element used in the SRM reference material and the most concentrated element in Orion and second most concentrated one in Sirius, had the smallest error bars. In summary, uncertainties are dominated by measuring statistics and calibration errors. Increasing counting time would decrease the former, while using appropriately prepared multielement reference materials would effectively remove the latter.

ISDC RESULTS

A series of four measurement campaigns in 2008 and 2010, followed by a reference material quantification run in 2011, were performed through ESRF proposal requests, on the ID22NI and ID22 beam lines. Given the highly oversubscribed access to these beam lines, we had to optimize our beam time, avoiding detailed time-consuming high-resolution, high-statistics mapping of all the tracks, and instead focused on the most promising ISDC.

Of the eight ISDC impact features containing several terminal particles and nonnegligible elemental track heterogeneity, using criteria akin to the candidacy levels defined in Westphal et al. (2014b), we rated seven of these as either moderate- or low-probability candidates based on XRF and sometimes XRD data as indicated in Table 1. Comparison with the CI chondritic abundances, considered representative of the bulk elemental composition of the solar system, highly volatile elements excepted, was judged as a vetoing criterion when several orders of magnitude differences in the mass ratio of elements to Fe mass were recorded. We propose the following criteria as indications of a particle's extraterrestrial versus terrestrial origin

1. If cerium is present, particles were most likely debris of the Stardust solar panels containing Ce-rich glass.
2. Se/Fe and Br/Fe overall ratios higher by a factor of 1000 or more than CI would disqualify these particles from being extraterrestrial.
3. As particles with volatile element (S, Cl, K, Cu, Zn, Ga) ratios to Fe should behave similarly following any heating event, all inconsistently depleted or enhanced ones would be disqualified from being extraterrestrial.

Elemental abundances derived from our XRF analyses are necessary, but not sufficient, to determine the interstellar origin of particles. Using the above veto criteria and our results, we present the analyses of seven tracks in Table 1. Isotopic analyses, to be carried out after the ISPE, will be required to definitively test whether particles are interstellar or not; therefore, here, we only report tentative results. Track I1027, 1,9, originally tentatively identified as an interstellar candidate, was mapped in detail and presented elsewhere (see Westphal et al. 2010). However, it was later removed from the ISDC list due to its high Ca/Fe and Zn/Fe ratios. The particles showing six or more element ratios to Fe higher by one or more orders of magnitude were labeled as having a "low" probability of being of

Table 1. Analyses of element to Fe ratios of raw counts in the K lines of seven tracks versus the CI chondritic mass ratios.

Summary of seven track analyses: element/Fe abundances compared with CI chondritic ones																	
Tracks–Elem./Fe	S	Cl	K	Ca	Sc	Ti	V	Cr	Mn	Ni	Cu	Zn	Se	Br	Analyses	Results	IS prob.
I1093,1,12,0,0	4.65E−02	4.34E−02	1.09E−01	2.91E−02	n.d.	5.40E−03	3.41E−03	1.39E−01	8.25E−03	3.32E−03	3.71E−03	2.47E−03	n.d.	5.29E−04	XRF	Cr, Cu,	Moderate
err. (1 σ)	1.08E−02	4.20E−03	3.73E−03	1.56E−03	n.d.	5.69E−04	3.76E−04	1.66E−03	5.81E−04	4.53E−03	1.80E−04	1.32E−04	n.d.	6.09E−05		Br ≫ CI	
I1081,1,13,0,0	1.65E+01	7.32E+00	n.d.	5.79E+00	n.d.	4.10E−01	5.65E−02	3.73E−02	3.43E−02	6.11E+00	1.80E−01	1.04E+00	3.73E−02	1.21E−02	XRF	Ti, V, Cu,	Low
err. (1 σ)	1.27E−01	4.48E−02	n.d.	2.29E−02	n.d.	4.38E−03	2.61E−03	1.49E−03	4.19E−03	1.28E−03	1.24E−03	3.70E−03	4.59E−04	3.31E−04		Zn Se, Br ≫ CI	
I1059,1,14,0,0	6.88E+01	4.31E+02	n.d.	5.42E+00	n.d.	8.18E−01	2.99E−01	3.51E−01	2.92E−01	1.09E+00	5.56E−01	1.98E+00	1.20E+00	2.95E−01	XRF	Ti, V, Cu,	Low
err. (1 σ)	5.03E+00	1.80E+01	n.d.	3.48E−01	n.d.	1.25E−01	8.92E−02	8.92E−02	5.21E−02	5.34E−02	3.28E−02	8.62E−02	5.39E−02	1.81E−02		Zn Se, Br ≫ CI	
I1029,5,15,0,0	1.43E+01	4.02E+01	4.41E+00	2.55E+00	n.d.	6.26E−01	1.90E−02	1.03E−02	n.d.	5.34E−02	2.47E+00	1.76E+00	3.01E−02	9.78E−02	XRF	Ti, V, Cu,	Low
err. (1 σ)	2.05E+00	1.64E+00	3.52E−01	1.54E−01	n.d.	5.60E−02	2.54E−02	1.70E−02	n.d.	8.71E−03	8.49E−02	6.15E−02	5.08E−03	7.38E−03		Zn Se, Br ≫ CI	
I1027,1,9	9.53E+00	2.38E+01	4.16E+00	2.26E+00	3.00E−01	1.44E+00	1.29E−01	2.25E−01	1.20E−01	6.58E−02	5.04E−01	4.34E−03	3.92E−02	1.59E+00	XRF,	Cl, Ca,	Low
err. (1 σ)	2.56E−01	1.76E−01	5.89E−02	2.56E−02	1.30E−02	1.51E−02	7.46E−03	5.74E−03	4.34E−03	2.13E−03	4.17E−03	4.34E−03	2.78E−03	9.48E−03	XRD XANES	Ti, V, Cu, Zn, Br ≫CI	
I1006,1,5,0,0	Ce debris–secondary ejecta from solar panel														XRF, XANES		Null
I1004,2,3,0,0	Ce debris–secondary ejecta from solar panel														XRF		Null
CI/Fe	2.89E−01	3.77E−03	2.94E−03	4.98E−02	3.19E−05	1.43E−02	2.94E−04	1.43E−02	1.04E−02	5.84E−02	7.08E−04	1.75E−03	1.10E−04	1.76E−05			
err. (1 σ)	1.69E−02	5.77E−04	1.71E−04	2.91E−03	1.86E−06	6.08E−04	1.71E−05	6.08E−04	4.43E−04	2.48E−03	7.39E−05	1.82E−04	8.36E−06	1.84E−06			

Table 2. X-ray fluorescence cross sections σ_{fluo} of elements at 17 keV incident energy and absolute number of counts integrated in the peaks of elements, with statistical errors including fitting at the 1σ level as reported by the PyMCA code.

Elem.	Z	σ_{fluo} (cm^2 g^{-1})	Orion		Sirius	
			Counts	±	Counts	±
Cl	17	0.87	199	16	512	24
Ca	20	1.45	246	17	46	8
Ti	22	4.18	246	22	5	8
V	23	5.38	392	23	31	8
Cr	24	7.00	4574	73	124	13
Mn	25	8.58	5139	82	3021	60
Fe	26	10.72	176626	427	16051	133
Co	27	12.68	1687	94	3707	75
Ni	28	15.62	18347	141	94249	311
Cu	29	17.49	4659	74	5971	89
Zn	30	20.42	188	18	708	31
Se	34	31.35	645	28	1009	33
Br	35	35.25	103	13	31	8

extraterrestrial origin, whereas the one having only three such element ratios was labeled as having a "moderate" probability of being of extraterrestrial origin.

SIRIUS AND ORION ELEMENTAL ABUNDANCES

Following the analyses of the seven tracks presented above as having a low probability of being ISDC, we present the XRF results of the two terminal particles of Track 30. For the analyses of these two particles, the beam intensity was tuned down to produce a fluence below the one in our previously established limit (Simionovici et al. 2011) to avoid sample damage and detector saturation. This limit is based on the minimum expected dose of X-rays experienced by interstellar dust in the interstellar medium, approximately 60 J cm^{-3}, hereafter referred to as the astrophysical limit (AL). Using the ESRF beam energy of 17 keV and the ID22NI nanoprobe beam spot, this yields a fluence of about 3×10^{19} ph cm^{-2}. As our flux here was 1–2.5 × 10^{10} ph s^{-1} in the beam spot, the above-mentioned MDLs were increased accordingly by up to two orders of magnitude. The nanoprobe maps reveal two terminal particles at the end of the track, "Orion" of about 131 pixels or 2.37 μm^2 surface at the terminus of the track, and "Sirius" of about 122 pixels or 2.21 μm^2, located 3 μm upstream. These particles may have been a single aggregate and split into two subgrains between X-ray analyses at the ID13 beam line at the ESRF (see Brenker et al. [2014] and Gainsforth et al. [2014]) and STXM low-energy analyses at the 11.0.2 beam line of the ALS (see Butterworth et al. 2014).

Table 3. Matrix minerals, number of moles, and total masses/densities assigned to the Orion and Sirius particles.

Matrix	Number of moles (10^{-15})	Mass (fg)	ρ (g cm^{-3})
Orion			
Fe	0.87	1195 ± 250	0.57
MgO	8.33		
Al_2O_3	7.87		
Sirius			
Mg_2 SiO_4	6.25	908 ± 125	0.2
Fe	0.079		

The two particles showed different chemical compositions (Fig. 1). Orion had a high Fe/Ni ratio, whereas that of Sirius was relatively low, as shown by the total counts and mass fractions in Tables 2 and 3, respectively. Chemical and structural heterogeneities at the submicrometer scale were not observed within the Sirius particle, in contrast to the Orion particle (Fig. 1). Orion was composed of a core depleted in heavy elements surrounded by an irregular and chemically heterogeneous mantle. Hundred nanometer sized zones were enriched, in particular, in transition elements, such as Fe, Ni, Cr, Mn, and Cu-, Co-, Ca-, V-, and Ti-rich phases could also be distinguished (Fig. 2).

SIRIUS AND ORION RESULTS

As an example of trace element quantification in Orion and Sirius, the Zn, Co, and Cu X-ray line assignment of relatively low-statistics lines is shown in Fig. 3.

For both Orion and Sirius, quantitative analysis was carried out using their average spectra per pixel, together with the aerogel average spectrum per pixel, normalized to the incident beam intensity. The average aerogel spectrum was subtracted from each particle average spectrum to obtain the final background-subtracted spectra, used in the subsequent quantification. Subtraction of the average aerogel spectrum introduces additional error calculated by adding in quadrature errors of individual spectra, based on Poisson counting statistics. Sum spectra are presented in Fig. 4 to estimate the importance of this correction, which sometimes fully cancels out elemental contributions such as Pb (a setup artifact, present in the station shielding) or Ar and Kr from the air. For Orion and Sirius, the S counts also cancel out after subtraction.

Table 2 presents the raw counts and 1σ errors, derived for all fitted elements in the two particles, as well as the X-ray fluorescence cross sections, from our Xraylib database (Brunetti et al. 2004), to help infer linearly dependent rough mass fraction values.

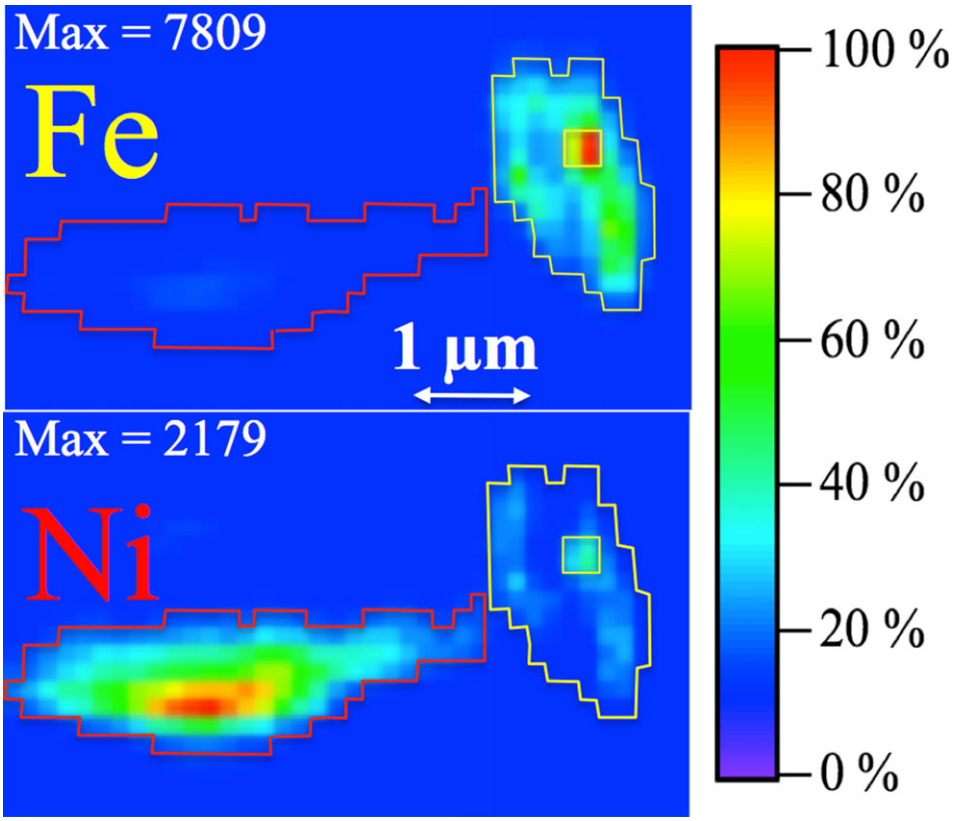

Fig. 1. Rainbow color-coded raw counts of K-shell fluorescence lines (normalized to maxima), showing chemical heterogeneity of Fe-rich Orion (right, yellow outline) and relative homogeneity of Ni-rich Sirius (left, red outline).

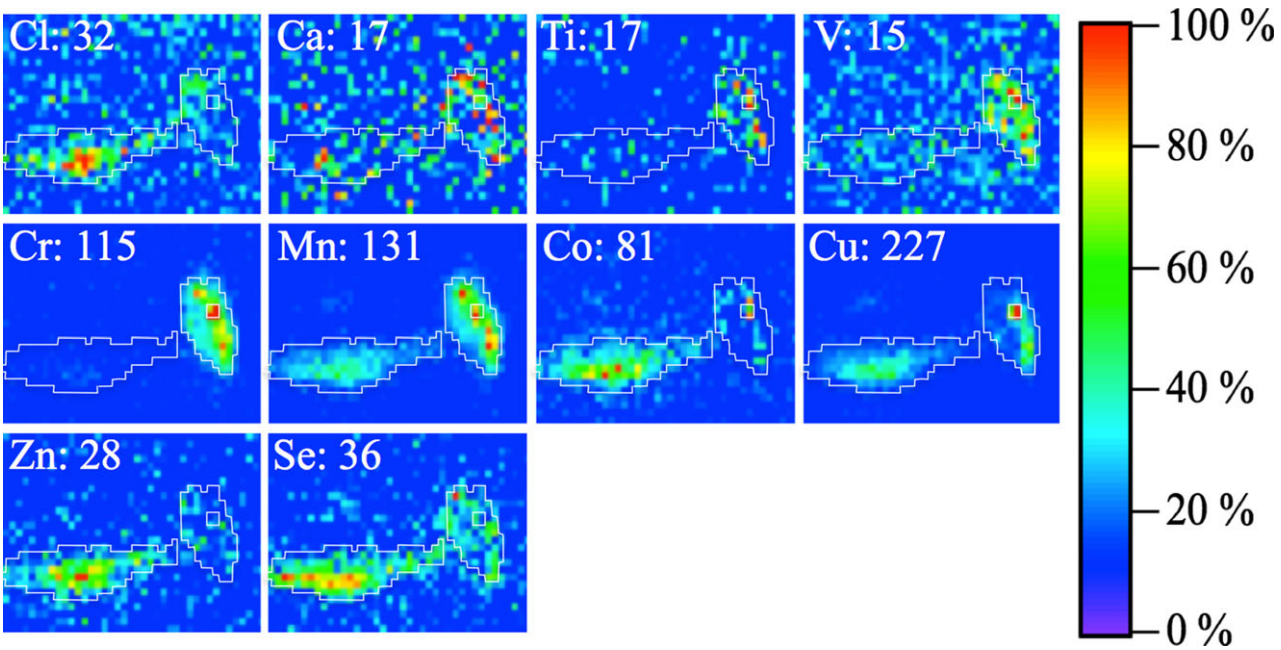

Fig. 2. Rainbow color-coded raw counts of K-shell fluorescence lines (normalized to maxima), showing elemental abundance maps of the Sirius and Orion particles, versus the outlines of the Fe and Ni distributions from Fig. 1.

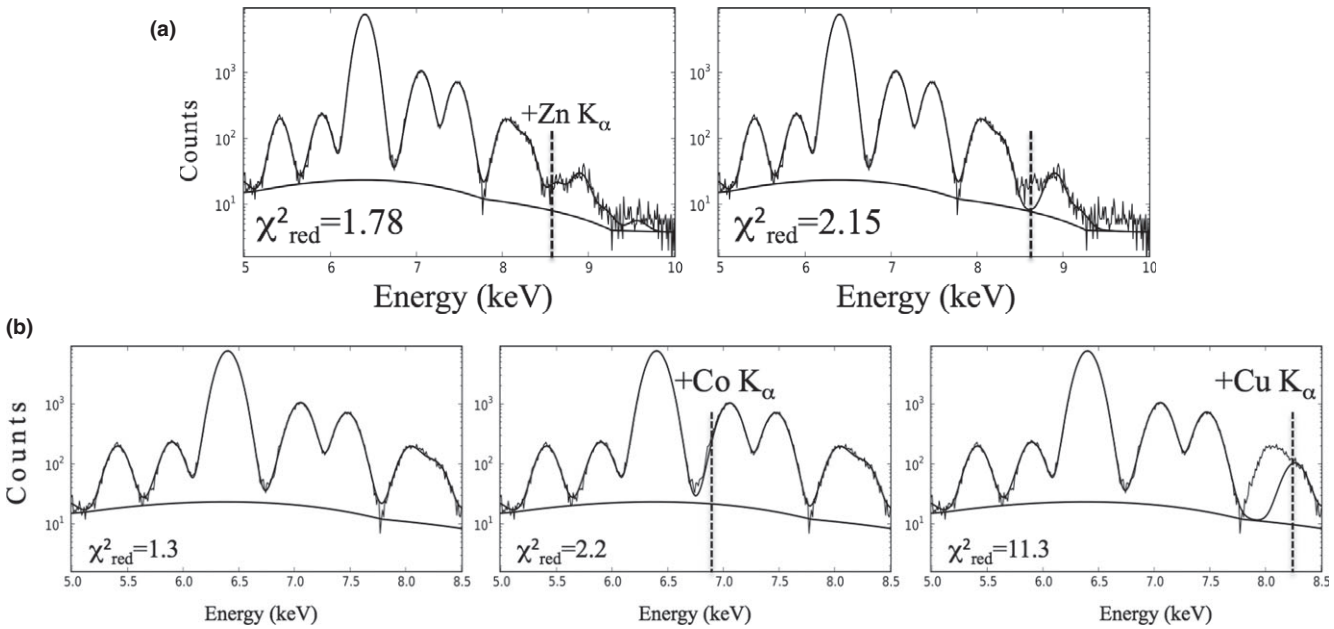

Fig. 3. a) X-ray lines fitted using PyMCA, showing that the reduced χ^2 goodness of fit criterion improves as the Zn K_α line is included in the fit. The left figure includes Zn in the fit and clearly is a better match to the data, while the right one assumes no Zn contribution. b) Spectra fitted with PyMCA, showing that the reduced χ^2 goodness-of-fit criterion improves as the Co and Cu K_α lines are included in the fit. The left figure includes both Co and Cu, the middle one no copper contribution, and the right one no cobalt contribution to the fit.

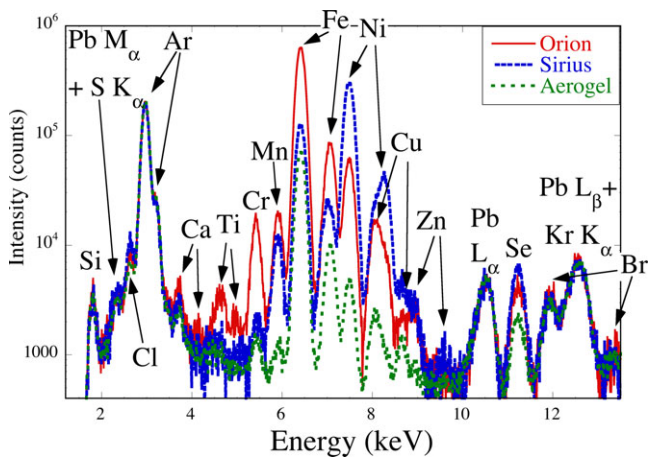

Fig. 4. Spectra of Orion, Sirius, and aerogel summed over 131, 122, and 754 pixels, respectively. All element characteristic lines were $K_\alpha + K_\beta$ except where labeled differently.

SIRIUS AND ORION ELEMENTAL COMPOSITION DEPENDENCE ON THE MATRIX CHOICE

XRF fluorescence maps helped us to achieve qualitative element analysis for atomic numbers $Z > 14$. To perform a quantitative analysis, one needs mass calibration standards and a sample matrix definition. As explained in the XRF analysis paragraph, the matrix attenuates the element lines and contributes to the sample total mass, by means of the undetected low Z elements; therefore, in PyMCA, one uses it to calculate mass fractions. Element masses were assigned to compositional phases present in the two particles by combining our high Z quantitative analysis with lower Z analyses, performed by STXM (Butterworth et al. 2014). Hereafter, we assume that all detected elements were combined into these several phases, thereby neglecting sulfides, pure metal phases (with the exception of Fe), or nonstoichiometric minerals. Therefore, the matrix is only an approximation used for absolute element quantification.

Orion was shown by STXM to be composed of 425 ± 25 fg of Al and 200 ± 40 fg of Mg assigned by Al and Mg X-ray absorption near edge structure (XANES) to spinel, although mostly amorphous with an average density of approximately 0.57 g cm^{-3}. The XRD maps of both particles acquired simultaneously with the XRF ones produced assignments of several spinel crystallites (see Gainsforth et al. 2014). We assume that all iron was present as metallic phases or in olivine, as we do not see any S in our spectra to suggest sulfides. Sirius was made of 300 ± 40 fg of Mg assigned to amorphous forsterite and free Fe with an average density of approximately 0.2 g cm^{-3} (see Butterworth et al. 2014). We verified that total heavy element masses

(approximately 59 fg for Orion and approximately 33 fg for Sirius) were, in both cases, negligible with respect to those of the low Z elements. As a consequence, the total densities must not be significantly different from the ones estimated using the low-Z analyses.

For Orion, we solve a system of equations, which assigns Mg and Al concentrations measured by STXM (Butterworth et al. 2014) as oxides MgO and Al_2O_3, and Fe from our XRF measurements as free iron. The parameters in the equations were the element total masses and the number of moles "*n*" by which one multiplies the known molar masses of the minerals to obtain the total masses of the particles. Of all mathematical solutions of the system of equations for the matrices, only three yield nonnegative results and reasonable total particle masses: the Fe metal, forsterite, magnesia and alumina, or spinel. In agreement with the STXM and XRD data (see Butterworth et al. [2014] and Gainsforth et al. [2014]), we used the following matrices for the element quantification:

$$\text{Orion} \Leftrightarrow n_{\text{Fe}} \cdot \text{Fe} + n_{\text{MgO}} \cdot \text{MgO} + n_{\text{Al}_2\text{O}_3} \cdot \text{Al}_2\text{O}_3$$

$$\begin{cases} \text{Al total mass (STXM)}: \ 425\text{fg} = \text{A}_{\text{Al}} \cdot n_{\text{Al}_2\text{O}_3} \cdot 2 \\ \text{Mg total mass (STXM)}: \ 200\text{fg} = \text{A}_{\text{Mg}} \cdot n_{\text{MgO}} \\ \text{Fe total mass (SR} - \text{XRF)}: \ 49\text{fg} = \text{A}_{\text{Fe}} \cdot n_{\text{Fe}} \end{cases}$$

$$\begin{aligned} \text{Orion total mass} &= m_{\text{Al}} + m_{\text{Mg}} + m_{\text{Fe}} + n_{\text{MgO}} \cdot \text{A}_{\text{O}} \\ &\quad + n_{\text{Al}_2\text{O}_3} \cdot 3 \cdot \text{A}_{\text{O}} \\ &= 1195 \text{ fg} \end{aligned}$$

and

$$\text{Sirius} \Leftrightarrow n_{\text{Fe}} \cdot \text{Fe} + n_{\text{Fo}} \cdot \text{Mg}_2\text{SiO}_4$$

$$\begin{cases} \text{Mg total mass (STXM)}: 300\text{fg} = \text{A}_{\text{Mg}} \cdot n_{\text{Fo}} \\ \text{Fe totalmass(SR} - \text{XRF)}: 5fg = \text{A}_{\text{Fe}} \cdot n_{\text{Fe}} \end{cases}$$

$$\begin{aligned} \text{Sirius total mass} &= m_{\text{Fe}} + m_{\text{Fo}} \\ &\quad + n_{\text{Fo}} \cdot (A_{\text{Si}} + 4 \cdot A_O) \\ &= 908 \text{ fg} \end{aligned}$$

These mineral assemblages and total masses were used as possible matrices to iterate the results of our fits of element concentrations. The different matrices yield different X-ray lines absorption coefficients, different element mass fractions, and total particle masses. After three iterations, convergence was achieved for the values in Table 3 with a few percent variations in all fitted element concentrations from Table 2. Sirius was modeled using the Mg and Si in the STXM results and our low-Fe signal, combined into a low-iron matrix, of amorphous nature again, given the lack of any XRD signal. If Fe is incorporated into an amorphous silicate of fayalite-bearing olivine composition (given the lack of any diffraction signal) instead of as Fe metal and forsterite in both particles, the particle total masses change by less than 5%, quite small compared with the systematic uncertainties associated with tabulated cross sections. For Orion, using alumina and magnesia as the approximation for the matrix composition allowed for the possibility of nonstoichiometric spinel.

Using the matrices from Table 3, we report total elemental mass abundances (>10 ppm) of both particles in Table 4 for the heavy elements ($Z \geq 17$), normalized to the Fe mass. We only use the measured Fe content of our particles for the normalization. This guarantees that the internal normalization cancels out common sources of error. The quoted errors do not include the total mass errors of approximately 20%, from Table 3.

In Orion, the total mass of the heavy elements was about 59 fg. We thus consider Fe to be a minor component, while Ni, Cr, and Mn were more than one order of magnitude lower (>1000 ppm). The characteristic value of the elemental Fe/Ni ratio was about 14. Finally, the element ratios to Fe were close to those of CI chondrites for Ca, Ti, Co, and Ni, but not for the volatile elements Br, Cu, and Zn.

As our samples were optically thin in the hard X-ray regime, the quantification results were fairly insensitive to the different correction terms of the respective matrices. In Sirius, the total mass of the heavy elements was about 33 fg. Ni was a major component and Fe, Cl, Mn, Co, and Cu were minor elements. The Fe/Ni ratio was about 0.25. However, elemental maps show that minor elements can be concentrated up to ten times in the submicrometer zones described above, indicating that total minor abundances can locally reach major abundances.

To address the possibility of these two particles having been an aggregate, prior to our analyses, we investigated their elemental abundance correlations. Figure 5 shows four element correlations for Orion (left panel) and Sirius (right panel).

One readily notices a correlation discrepancy for Fe and Ni (the major element of each particle) between Sirius and Orion, whereas Cr, Mn, and Cu appear relatively well correlated with their respective major element in both particles. Correlations being scale-dependent, this may also point out a smaller correlation scale, not apparent at our beam size resolution.

Finally, Orion's element ratios to Fe were close to those of the CIs for Ca, Ti, Co, and Ni, but not for the highly volatile elements Br, Cu, Zn.

DISCUSSION

The heavy element analyses presented here supplement our present understanding of the composition

Table 4. Elemental mass ratios to Fe of Orion based on the Fe + alumina + magnesia matrix as well as of Sirius based on the Fe + forsterite matrix, with errors at the 1σ level. Fe absolute masses and errors are shown for completeness. Ratios to Fe and errors for solar CI values are from Lodders et al. (2009).

	Orion		Sirius			
	$Fe + MgO + Al_2O_3$		$Fe + Mg_2SiO_4$			
	mass = 1195 fg		mass = 908 fg		CI	
Elem.	Ratio to Fe	± (%)	Ratio to Fe	± (%)	Ratio to Fe	± (%)
Cl	0.0249	11	0.8825	8	0.0038	15
Ca	0.0066	10	0.0233	19	0.0498	5
Ti	0.0037	11	0.0107	141	0.0024	8
V	0.0044	9	0.0075	26	0.0003	5
Cr	0.0406	7	0.0140	13	0.0143	3
Mn	0.0368	7	0.2393	7	0.0104	3
Co	0.0091	9	0.1929	7	0.0027	3
Ni	0.0696	7	3.9257	7	0.0584	3
Cu	0.0157	7	0.2210	7	0.0007	10
Zn	0.0004	12	0.0245	8	0.0018	10
Se	0.0014	8	0.0314	8	0.0001	7
Br	0.0002	14	0.0020	27	0.00002	15
Elem.	mass (fg)	± (%)	mass (fg)	± (%)	mass (ppm)	± (%)
Fe	48.9	3	5	12	185000	3

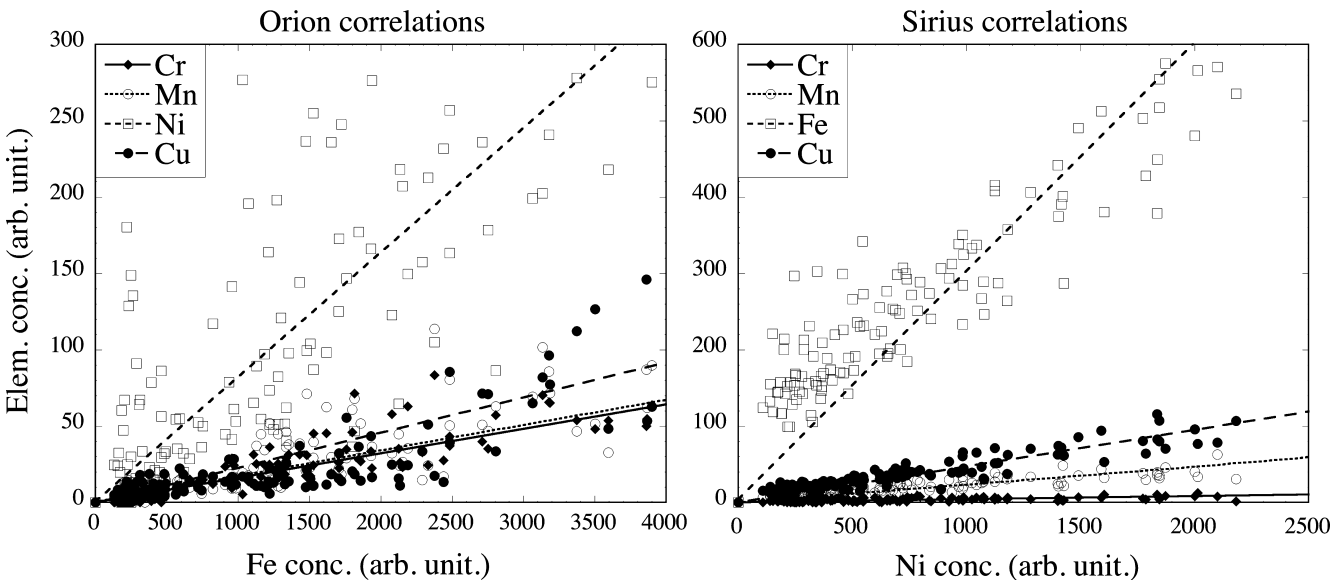

Fig. 5. Orion and Sirius element abundance correlations relative to major element Fe and Ni, respectively. Lines are linear fits to the data.

of Orion and Sirius, the two particles present in the track at the time of our analysis. The micrometer size of the Orion particle or its putative original assemblage observed by XRF imaging (see Brenker et al. 2014) was large compared with the model size distribution of the interstellar dust (Weingartner and Draine [2001] and Draine [2003]). However, similar in situ dust grain sizes were already measured inside the solar system (Grün et al. 1994) or reported based on observations from the dust detectors on Ulysses and Galileo (Van Dishoeck 2004).

The XRF heavy element images reveal a rather complex structure of Orion, with a homogeneous depleted core and numerous 200 nm size heterogeneities. Our simultaneously acquired XRD topographs are consistent with this picture of a mantle corresponding to sparse spinel crystallites (<100 nm) around the core of Orion (Gainsforth et al. 2014). Given the average density

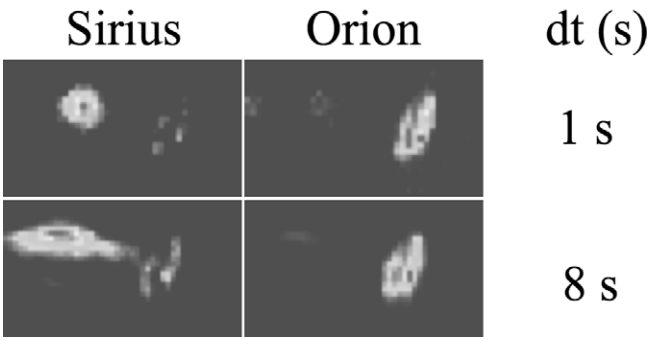

Fig. 6. Sirius and Orion total fluorescence successive scans with short (1 s) and long (8 s) dwell time (dt) for alignment and good statistics, respectively, showing Sirius spread out due to overexposure (lower).

of spinel, the compactness of the grains must be very low. However, such a fluffy nature and sizes of about 200 nm are consistent with the properties expected for interstellar dust grains (Draine 2003).

Abundances reported for minor and major elements in these two particles show Ca/Fe, Ti/Fe, Co/Fe, and Ni/Fe ratios close to those of chondrites for Orion. The elemental abundances were possibly changed by multiple processing events undergone by the two particles, *during* and *after* their capture in the Stardust aerogel. After the initial measurement campaign performed by Brenker et al. (2014), Butterworth et al. (2014) detected the loss of approximately 95% of the Fe mass from the originally observed single particle and its redistribution in an unknown disruption event in the neighboring aerogel track. In the ID22NI XRF/XRD measurements we performed after measurements of Brenker et al. (2014), we observed a strong depletion of Fe, yet Orion still showed approximately 200 nm sized crystalline phases (Gainsforth et al. 2014). A second disruption event occurred when the beam dwell time was set to 8 seconds per point, thus yielding a factor of overexposure in the fluence of between 7 (for a beam spot of size ± FWHM) and 10 (beam spot of size ± 3σ) higher than the AL. The result was spatial smearing of Sirius, which allowed us to interpret the relative homogeneity in the major element distribution of Sirius on a three times larger area. For Orion, on the other hand, no noticeable size variation or halo distribution of other elements around its contour was detected, confirming that it must have remained fairly unaltered.

No change in the composition of Sirius or its local chemistry (oxidation state, coordination, etc.) was observed after the smearing. This is substantiated by our previous low-resolution fast scans shown in Fig. 6 and by the Al XANES scans performed at ALS (see Butterworth et al. 2014) before and after our measurement campaign. Therefore, our observations indicate that Sirius was a highly altered particle, with many differences in elemental concentrations from Orion. The 200 nm sizes and the heterogeneity of the minor heavy elements concentrated in single pixels in the mantle of Orion may be interpreted as reflecting genuinely different spinel populations.

CONCLUSIONS

Our results demonstrate the usefulness of synchrotron hard X-ray fluorescence as a preliminary screening tool to determine the elemental abundances in the Z = 15–30 range in submicron particles embedded in Stardust aerogel. They allow identification of anthropogenic contaminants with a high degree of confidence and also interstellar candidates exhibiting compositions consistent with interstellar or interplanetary dust. Seven interstellar candidate impact features from the SIDC aerogel collection were ruled out as having an interstellar origin, based on elemental composition arguments. We produced an absolute quantification of elemental abundances in the two grains observed in the track I1043,1,30,0,0, Orion and Sirius, which were most likely to have an origin in the local interstellar medium.

A set of corrections of the beam parameters, reference materials, and fundamental atomic parameters was applied and evaluated. In particular, the matrix corrections were carried out in coordination with STXM analyses at the 10.3.2 ALS beam line before and after every hard X-ray XRF analysis (see Butterworth et al. 2014) and were found to be minor compared with other uncertainties. Based on our simultaneous XRD analyses (see Gainsforth et al. 2014), Orion was inferred to consist of a mineral assemblage of forsterite, spinel, and an Fe-bearing phase. A strong Fe depletion and the size variation and halo distribution of heavy elements show that Sirius was a highly altered particle, whereas Orion most likely remained relatively unaltered.

Acknowledgments—A. Simionovici and L. Lemelle acknowledge support from the French "Centre National d'Etudes Spatiales" (CNES). The Stardust mission was supported by NASA as the fourth mission in the Discovery program.

Editorial Handling—Dr. A. J. Timothy Jull

REFERENCES

Bleuet P., Simionovici A., Lemelle L., Ferroir T., Cloetens P., Tucoulou R., and Susini J. 2008. Hard X-rays nanoimaging for Earth and planetary science samples. *Applied Physics Letter* 92:213111-1–213111-3.

Brenker F. E., Schoonjans T., Silversmit G., Vekemans B., Vincze L., Westphal A. J., Allen C., Anderson D., Ansari A., Bajt S., Bastien R. S., Bassim N., Bechtel H. A., Borg J., Bridges J., Brownlee D. E., Burchell M., Burghammer M., Butterworth A. L., Changela H., Cloetens P., Davis A. M., Doll R., Floss C., Flynn G., Fougeray P., Frank D., Gainsforth Z., Grün E., Heck P. R., Hillier J. K., Hoppe P., Hudson B., Huth J., Hvide B., Kearsley A.-t., King A. J., Lai B., Leitner J., Lemelle L., Leroux H., Leonard A., Lettieri R., Marchant W., Nittler L. R., Ogliore R., Ong W. J., Postberg F., Price M. C., Sandford S. A., Tresseras J.-A. S., Schmitz S., Simionovici A. S., Grün E., Solé V. A., Srama R., Stephan T., Sterken V., Stodolna J., Stroud R. M., Sutton S., Trieloff M., Tsou P., Tsuchiyama A., Tyliszczak T., Von Korff J., Wordsworth N., Zevin D., Zolensky M. E., and >30,000 Stardust@home dusters. 2014. Stardust Interstellar Preliminary Examination VII: XRF analyses of interstellar dust candidates at ESRF ID13. *Meteoritics & Planetary Science*, doi:10.1111/maps.12206.

Brownlee D., Tsou P., Aléon J., Alexander C. M. O'D., Araki T., Bajt S., Baratta G. A., Bastien R., Bland P., Bleuet P., Borg J., Bradley J. P., Brearley A., Brenker F., Brennan S., Bridges J. C., Browning N. D., Brucato J. R., Bullock E., Burchell M. J., Busemann H., Butterworth A., Chaussidon M., Cheuvront A., Chi M., Cintala M. J., Clark B. C., Clemett S. J., Cody G., Colangeli L., Cooper G., Cordier P., Daghlian C., Dai Z. R., D'Hendecourt L., Djouadi Z., Dominguez G., Duxbury T., Dworkin J. P., Ebel D. S., Economou T. E., Fakra S., Fairey S. A. J., Fallon S., Ferrini G., Ferroir T., Fleckenstein H., Floss C., Flynn G. J., Franchi I. A., Fries M., Gainsforth Z., Gallien J.-P., Genge M., Gilles M. K., Gillet P., Gilmour J., Glavin D. P., Gounelle M., Grady M. M., Graham G. A., Grant P. G., Green S. F., Grossemy F., Grossman L., Grossman J. N., Guan Y., Hagiya K., Harvey R., Heck P., Herzog G. F., Hoppe P., Hörz F., Huth J., Hutcheon I. D., Ignatyev K., Ishii H., Ito M., Jacob D., Jacobsen C., Jacobsen S., Jones S., Joswiak D., Jurewicz A., Kearsley A. T., Keller L. P., Khodja H., Kilcoyne A. L. D., Kissel J., Krot A., Langenhorst F., Lanzirotti A., Le L., Leshin L. A., Leitner J., Lemelle L., Leroux H., Liu M.-C., Luening K., Lyon I., MacPherson G., Marcus M. A., Marhas K., Marty B., Matrajt G., McKeegan K., Meibom A., Mennella V., Messenger K., Messenger S., Mikouchi T., Mostefaoui S., Nakamura T., Nakano T., Newville M., Nittler L. R., Ohnishi I., Ohsumi K., Okudaira K., Papanastassiou D. A., Palma R., Palumbo M. E., Pepin R. O., Perkins D., Perronnet M., Pianetta P., Rao W., Rietmeijer F. J. M., Robert F., Rost D., Rotundi A., Ryan R., Sandford S. A., Schwandt C. S., See T. H., Schlutter D., Sheffield-Parker J., Simionovici A., Simon S., Sitnitsky I., Snead C. J., Spencer M. K., Stadermann F. J., Steele A., Stephan T., Stroud R., Susini J., Sutton S. R., Suzuki Y., Taheri M., Taylor S., Teslich N., Tomeoka K., Tomioka N., Toppani A., Trigo-Rodríguez J. M., Troadec D., Tsuchiyama A., Tuzzolino A. J., Tyliszczak T., Uesugi K., Velbel M., Vellenga J., Vicenzi E., Vincze L., Warren J., Weber I., Weisberg M., Westphal A. J., Wirick S., Wooden D., Wopenka B., Wozniakiewicz P., Wright I., Yabuta H., Yano H., Young E. D., Zare R. N., Zega T., Ziegler K., Zimmerman L., Zinner E., and Zolensky M. 2006. Comet 81P/Wild 2 under a microscope. *Science* 314:1711–1716.

Brunetti A., Sanchez del Rio M., Golosio B., Simionovici A., and Somogyi A. 2004. A library for X-ray-matter interaction cross sections for X-ray fluorescence applications. *Spectrochimica Acta B* 59:1725–1731.

Butterworth A. L., Westphal A. J., Tyliszczak T., Gainsforth Z., Stodolna J., Frank D., Allen C., Anderson D., Ansari A., Bajt S., Bastien R. S., Bassim N., Bechtel H. A., Borg J., Brenker F. E., Bridges J., Brownlee D. E., Burchell M., Burghammer M., Changela H., Cloetens P., Davis A. M., Doll R., Floss C., Flynn G., Grün E., Heck P. R., Hillier J. K., Hoppe P., Hudson B., Huth J., Hvide B., Kearsley A., King A. J., Lai B., Leitner J., Lemelle L., Leroux H., Leonard A., Lettieri R., Marchant W., Nittler L. R., Ogliore R., Ong W. J., Postberg F., Price M. C., Sandford S. A., Sans Tresseras J.-A., Schmitz S., Schoonjans T., Silversmit G., Simionovici A. S., Solé V. A., Srama R., Stephan T., Sterken V., Stroud R. M., Sutton S., Trieloff M., Tsou P., Tsuchiyama A., Vekemans B., Vincze L., Korff J. V., Wordsworth N., Zevin D., Zolensky M. E., and >30,000 Stardust@home dusters. 2014. X-ray absorption analyses of major rock- forming elements in candidate interstellar dust impacts by scanning transmission X-ray microscopy. *Meteoritics & Planetary Science*, doi:10.1111/maps.12220.

Draine B. T. 2003. Interstellar dust grains. *Annual Review of Astronomy and Astrophysics* 41:241–289.

Flynn G. J., Bleuet P., Borg J., Bradley J. P., Brenker F. E., Brennan S., Bridges J., Brownlee D. E., Bullock E. S., Burghammer M., Clark B. C., Dai Z. R., Daghlian C. P., Djouadi Z., Fakra S., Ferroir T., Floss C., Franchi I. A., Gainsforth Z., Gallien J.-P., Gillet P., Grant P. G., Graham G. A., Green S. F., Grossemy F., Heck P. R., Herzog G. F., Hoppe P., Hörz F., Huth J., Ignatyev K., Ishii H. A., Janssens K., Joswiak D., Kearsley A. T., Khodja H., Lanzirotti A., Leitner J., Lemelle L., Leroux H., Luening K., MacPherson G. J., Marhas K. K., Marcus M. A., Matrajt G., Nakamura T., Nakamura-Messenger K., Nakano T., Newville M., Papanastassiou D. A., Pianetta P., Rao W., Riekel C., Rietmeijer F. J. M., Rost D., Schwandt C. S., See T. H., Sheffield-Parker J., Simionovici A., Sitnitsky I., Snead C. J., Stadermann F. J., Stephan T., Stroud R. M., Susini J., Suzuki Y., Sutton S. R., Taylor S., Teslich N., Troadec D., Tsou P., Tsuchiyama A., Uesugi K., Vekemans B., Vicenzi E. P., Vincze L., Westphal A. J., Wozniakiewicz P., Zinner E., and Zolensky M. E. 2006. Elemental compositions of comet 81P/Wild 2 samples collected by Stardust. *Science* 314:1731–1735.

Frank D. R., Westphal A. J., Zolensky M. E., Bastien R. K., Gainsforth Z., Allen C., Anderson D., Ansari A., Bajt S., Bassim N., Bechtel H. A., Borg J., Brenker F. E., Bridges J., Brownlee D. E., Burchell M., Burghammer M., Butterworth A. L., Changela H., Cloetens P., Davis A. M., Doll R., Floss C., Flynn G., Grün E., Heck P. R., Hillier J. K., Hoppe P., Hudson B., Huth J., Hvide B., Kearsley A., King A. J., Lai B., Leitner J., Lemelle L., Leroux H., Leonard A., Lettieri R., Marchant W., Nittler L. R., Ogliore R., Ong W. J., Postberg F., Price M. C., Sandford S. A., Tresseras J. S., Schmitz S., Schoonjans T., Silversmit G., Simionovici A. S., Solé V. A., Srama R., Stephan T., Sterken V. J., Stodolna J., Stroud R. M., Sutton S., Trieloff M., Tsou P., Tsuchiyama A., Tyliszczak T., Vekemans B., Vincze L., Korff J. V., Wordsworth N., and Zevin D., and >30,000 Stardust@home dusters. 2013.

Stardust Interstellar Preliminary Examination II: Curating the interstellar dust collector, picokeystones, and sources of impact tracks. *Meteoritics & Planetary Science*, doi:10.1111/maps.12147.

Frisch P.C. and Slavin J. D. 2012. Interstellar dust close to the Sun. *Earth, Planets and Space* 65(3):175–182.

Gainsforth Z., Brenker F. E., Burghammer M., Simionovici A. S., Schmitz S., Cloetens P., Lemelle L., Sans Tresseras J.-A., Schoonjans T., Silversmit G., Solé V. A., Vekemans B., Vincze L., Westphal A. J., Allen C., Anderson D., Ansari A., Bajt S., Bastien R. S., Bassim N., Bechtel H. A., Borg J., Bridges J., Brownlee D. E., Burchell M., Butterworth A. L., Changela H., Davis A. M., Doll R., Floss C., Flynn G., Frank D., Gru n E., Heck P. R., Hillier J. K., Hoppe P., Hudson B., Huth J., Hvide B., Kearsley A., King A. J., Lai B., Leitner J., Leroux H., Leonard A., Lettieri R., Marchant W., Nittler L. R., Ogliore R., Ong W. J., Postberg F., Price M. C., Sandford S. A., Srama R., Stephan T., Sterken V., Stodolna J., Stroud R. M., Sutton S., Trieloff M., Tsou P., Tsuchiyama A., Tyliszczak T., Korff J. V., Wordsworth N., Zevin D., Zolensky M. E., and >30,000 Stardust@home dusters. 2014. Identification of crystalline material in two interstellar dust candidates from the Stardust mission. *Meteoritics & Planetary Science*, doi:10.1111/maps.12148.

Grün E., Gustafson B., Mann I., Baguhl M., Morfill G. E., Staubach P., Taylor A., and Zook H. A. 1994. Interstellar dust in the heliosphere. *Astronomy & Astrophysics* 286:915–924.

Jenkins E. B. 2008. A unified representation of gas-phase element depletions in the interstellar medium. *The Astrophysical Journal* 700:1299–1348.

Kimura H., Mann I., and Jessberger E. K. 2003. Elemental abundances and mass densities of dust and gas in the local interstellar cloud. *The Astrophysical Journal* 582:846–858.

Krause M.O., Nestor C.W., Jr., Sparks C. J., Jr., and Ricci E. 1978. *X-ray fluorescence cross sections for K and L X-rays of the elements*. OSTI ID: 7032250. Oak Ridge, Tennessee: U.S. Department of Commerce.

Lodders K. and Amari S. 2005. Presolar grains from meteorites: Remnants from the early times of the solar system. *Chemie der Erde* 65:93–166.

Lodders K. Palme H., and Gail H. P. 2009. Abundances of the elements in the solar system. *Landolt-Börnstein New Series*, Vol. VI/4B, edited by Trümper J. E. Berlin: Springer-Verlag. pp. 560–630.

Mann I. 2010. Interstellar dust in the solar system. *Annual Review of Astronomy and Astrophysics* 48:173–203.

Mumma M. J. and Charnley S. B. 2011. The chemical composition of comets—Emerging taxonomies and natal heritage. *Annual Review of Astronomy and Astrophysics* 49:471–524.

Schramm L. S., Brownlee D. E., and Wheelock M. M. 1989. Major element composition of stratospheric micrometeorites. *Meteoritics* 24:99–112.

Simionovici A., Allen C., Bajt S., Bastien R., Bechtel H., Borg J., Brenker F. E., Bridges J. C., Brownlee D. E., Burchell M. J., Burghammer M., Butterworth A., Cloetens P., Davis A. M., Floss C., Flynn G., Frank D., Gainsforth Z., Grün E., Heck P. R., Hillier J., Hoppe P., Howard L., Huss G. R., Huth J., Kearsley A. T., King A. J., Lai B., Leitner J., Lemelle L., Leroux H., Lettieri R., Marchant W., Nittler L., Ogliore R., Postberg F., Sandford S., Tresseras J. A. S., Schoonjans T., Schmitz S., Silversmit G., Sole V. A., Srama R., Stephan T., Stodolna J., Stroud R. M., Sutton S., Trieloff M., Tsou P., Tsuchiyama A., Tyliczs-Zak T., Vekemans B., Vincze L., Westphal A. J., Zevin D., and Zolensky M. E. 2011. Synchrotron radiation microprobe effects on Stardust interstellar dust candidates (abstract #2812). Lunar and Planetary Science Conference. CD-ROM.

Sofia U. J. and Meyer D. M. 2001. Interstellar abundance standards revisited. *The Astrophysical Journal* 554:221–224.

Sole V.A., Papillon E., Cotte M., Walter P., and Susini J. 2007. A multiplatform code for the analysis of energy-dispersive X-ray fluorescence spectra. *Spectrochimica Acta B* 62:63–68.

Tsou P., Brownlee D. E., Sandford S. A., Hörz F., and Zolensky M. E. 2003. Wild 2 and interstellar sample collection and Earth return. *Journal of Geophysical Research* 108:8113.

Van Dishoeck E. F. 2004. ISO spectroscopy of gas and dust: From molecular clouds to protoplanetary disks. *Annual Review of Astronomy and Astrophysics* 42:119–167.

Weingartner J. C. and Draine B. T. 2001. Dust grain size distributions and extinction in the Milky Way, LMC, and SMC. *The Astrophysical Journal* 548:296–309.

Westphal A. J., Butterworth A. L., Snead Ch. J., Craig N., and Anderson D. 2005. Stardust@Home: A massively distributed public search for interstellar dust in the Stardust Interstellar Dust Collector (abstract #1908). 36th Lunar and Planetary Science Conference. CD-ROM.

Westphal A. J., Allbrink A., Allen C., Bajt S., Bastien R., Bechtel H., Bleuet P., Borg J., Bowker S., Brenker F., Bridges J., Brownlee D. E., Burchell M., Burghammer M., Butterworth A. L., Campanile A., Cloetens P., Cody G., Ferroir T., Ferrari K., Floss C., Flynn G. J., Frank D., Gainsforth Z., Grün E., Harmer M., Hoppe P., Kearsley A., Kulkarni S., Lai B., Lemelle L., Leroux H., Lettieri R., Marchant W., Mccreadie B., Nittler L. R., Ogliore R., Postberg F., Rigamonti C., Sandford S. A., Schmitz S., Silversmit G., Simionovici A. S., Sperry G., Srama R., Stadermann F., Stephan T., Stroud R. M., Susini J., Sutton S., Thompson V., Toucoulou R., Trieloff M., Tsou P., Tsuchiyama A., Tyliczszak T., Vekemans B., Vincze L., Warren J., Yahnke T., Zevin D., and Zolensky M. E. 2010. Non-destructive search for interstellar dust using synchrotron microprobes. *AIP Conference Proceedings* 1221:131–138.

Westphal A. J., Allen C., Anderson D., Ansari A., Bajt S., Bechtel H. A., Borg J., Brenker F., Bridges J., Brownlee D. E., Burchell M., Burghammer M., Butterworth A. L., Cloetens P., Davis A. M., Floss C., Flynn G. J., Frank D., Gainsforth Z., Grün E., Heck P. R., Hillier J. K., Hoppe P., Howard L., Huss G. R., Huth J., Kearsley A., King A. J., Lai B., Leitner J., Lemelle L., Leroux H., Lettieri R., Lyverse P., Marchant W., Nittler L. R., Ogliore R. C., Postberg F., Price M. C., Sandford S. A., Sans Tresseras J. A., Schmitz S., Schoonjans T., Silversmit G., Simionovici A., Solé V. A., Srama R., Stadermann F. J., Stephan T., Stodolna J., Stroud R. M., Sutton S. R., Toucoulou R., Trieloff M., Tsou P., Tsuchiyama A., Tyliczszak T., Vekemans B., Vincze L., von Korff J., Zevin D., Zolensky M. E., and >29000 Stardust@home dusters. 2014a. Stardust Preliminary Examination: Final reports of the Stardust Interstellar Preliminary Examination. *Meteoritics & Planetary Science*, doi:10.1111/maps.12221.

Westphal A. J., Allen C., Anderson D., Ansari A., Bajt S., Bechtel H. A., Borg J., Brenker F., Bridges J., Brownlee D. E., Burchell M., Burghammer M., Butterworth A. L., Cloetens P., Davis A. M., Floss C., Flynn G. J., Frank D., Gainsforth Z., Grün E., Heck P. R., Hillier J. K., Hoppe P., Howard L., Huss G. R., Huth J., Kearsley A., King A. J., Lai B., Leitner J., Lemelle L., Leroux H., Lettieri R., Lyverse P., Marchant W., Nittler L. R., Ogliore R. C., Postberg F., Price M. C., Sandford S. A., Sans Tresseras J. A., Schmitz S., Schoonjans T., Silversmit G., Simionovici A., Solé V. A., Srama R., Stadermann F. J., Stephan T., Stodolna J., Stroud R. M., Sutton S. R., Toucoulou R., Trieloff M., Tsou P., Tsuchiyama A., Tyliczszak T., Vekemans B., Vincze L., von Korff J., Zevin D., Zolensky M. E., and >29000 Stardust@home dusters. 2014b. Stardust Interstellar Preliminary examination I: Identification of tracks in aerogel. *Meteoritics & Planetary Science*, doi:10.1111/maps.12168.